Research Article | Vol. 10, No. 7 | 1 Jul 2019 | BIOMEDICAL OPTICS EXPRESS 3301
Biomedical Optics EXPRESS

Spatiotemporally controlled nano-sized third harmonic generation agents

Dmitry Nevozhay,[1,2,8] Michael Weiger,[3,8] Peter Friedl,[3,4,5] and Konstantin V. Sokolov[1,6,7,*]

[1]*Department of Imaging Physics, The University of Texas MD Anderson Cancer Center, 1515 Holcombe Boulevard, Houston, TX 77030, USA*
[2]*School of Biomedicine, Far Eastern Federal University, 8 Sukhanova Street, Vladivostok, 690950, Russia*
[3]*Department of Genitourinary Medical Oncology, The University of Texas MD Anderson Cancer Center, 1515 Holcombe Boulevard, Houston, TX 77030, USA*
[4]*Department of Cell Biology, Radboud Institute for Molecular Life Sciences, Radboud University Medical Center, Nijmegen, Netherlands.*
[5]*Cancer Genomics Centre, (CGC.nl), 3584 Utrecht, Netherlands*
[6]*Department of Bioengineering, Rice University, 6100 Main St, Houston, TX 77005, USA*
[7]*Department of Biomedical Engineering, The University of Texas at Austin, 107 W Dean Keeton Street, Austin, TX 78712, USA*
[8]*Equal contribution*
**ksokolov@mdanderson.org*

Abstract: Here, we present a new class of third harmonic generation (THG) imaging probes that can be activated with precise spatiotemporal control using non-linear excitation. These probes consist of lipid-coated perfluorocarbon nanodroplets with embedded visible chromophores. The droplets undergo phase transition from liquid to gas upon heating mediated by two-photon absorption of NIR light by the embedded dyes. Resulting microbubbles provide a sharp, local refractive index mismatch, which makes an excellent source of THG signal. Potential applications of these probes include activatable THG agents for biological imaging and "on-demand" delivery of various compounds under THG monitoring.

1. Introduction

Advances in imaging technologies and respective contrast agents have greatly expanded our understanding of tissue structure, cell functions and interactions as well as subcellular events from basic cell biology to oncology [1–5]. Advanced microscopy exploits a range of contrast strategies to detect structural, molecular, and physical cell and tissue properties, and there is growing need for pairing of imaging modalities with innovative contrast agents.

Most contrast agents in life sciences today rely on the principle of single- or two-photon excitation. While these agents are extremely useful in generating imaging contrast, there are constraints in the number of unique targets that can be imaged due to spectral overlap in the visible light range. Additionally, scattering and absorption of both the visible excitation sources and emissions by the contrast agents present a challenge to 3D *in vitro* and *in vivo* imaging [6]. The development of multiphoton microscopy with pulsed near-red and infrared laser excitation sources enabled *in vivo* imaging of live cells and tissue structures at high resolution, low phototoxicity, and reasonable depth of penetration (300-1000 μm) [7–11]. Furthermore, the possibility of higher harmonic imaging by second harmonic generation (SHG) and third harmonic generation (THG) enables additional modes of endogenous tissue contrast and opportunities for development of exogenous contrast agents which report by fluorescence-independent mechanisms. SHG occurs when biological structures containing asymmetric repetitive units (e.g. striated muscle and collagen fibers) convert two photons of

#364132 https://doi.org/10.1364/BOE.10.003301
Journal © 2019 Received 4 Apr 2019; revised 5 Jun 2019; accepted 5 Jun 2019; published 13 Jun 2019

Biomedical Optics EXPRESS

an excitation light source into a single emitted photon at double the energy (1/2 of the excitation wavelength). THG occurs at interphases, typically with a refractive index mismatch (e.g. water-lipid/protein), that results in conversion of three photons of an excitation light into a single emitted photon with triple the energy (1/3 of the excitation wavelength) [12]. Whereas SHG is limited to asymmetry of the structure being imaged, THG is based on differences in refractive index and, hence, is more broadly applicable. Unlike fluorescence, THG does not suffer from photobleaching or generation of reactive oxygen species [12] and allows detection of intrinsic complex tissue structures with subcellular resolution, including interstitial tissue, cell surfaces, and microvesicles in live animals [13].

Such advantages prompted development of specific THG imaging contrast agents for specialized applications in life sciences requiring unique labeling or increased contrast. For biologically relevant THG imaging, these agents include lipid-enclosed quantum dots [14], lipid microbubbles [15], tattoo dye [16], porphyrin aggregates [17], bismuth ferrite [18] or titanium dioxide [19] nanoparticles. These constitutive THG probes can enable cell tracking applications [14,18], as well as molecular imaging through conjugation with targeting moieties, e.g., antibodies or peptides [15]. However, they also suffer from the complexity of THG signals originating in 3D tissue and the generic nature of the signal which might not be readily discriminated from the background. To increase specificity, activatable or externally triggered THG probes could offer new sensing capabilities in biomolecular imaging by creating on demand contrast or enabling image-guided interventions and delivery, not unlike activatable fluorescence probes [20–24]. Here we address this need by developing and initially validating spatiotemporal, inducible contrast probes for THG imaging that are based on phase changing perfluorocarbon (PFC) nanodroplets. We applied highly localized two-photon excitation to trigger phase-change of PFC nanodroplets and THG visualization of the resulting microbubbles post-excitation dynamics. The spatiotemporal precision of nanodroplet activation could allow utilization of these agents for spatially and temporally controlled on-demand image-guided delivery, which is not possible with previously reported agents.

The nanodroplets consist of a lipid-stabilized PFC core with embedded light absorbing dye molecules. Previously, these nanoparticles were used to create a high signal and contrast in photoacoustic imaging [25–27]. In these studies, excitation of the nanodroplets occurs with nanosecond laser pulses, which are matched with the absorption band of an embedded dye, followed by a liquid to gas transition of the PFC core which elicits a strong photoacoustic signal. Using this principle, we recently demonstrated that the phase changing PFC nanodroplets can also be used to create localized, high frequency elastic waves in optical coherence elastography measurements [28,29]. PFC with relatively low boiling temperatures, e.g. perfluoropentane or perfluorohexane, are generally used to facilitate the liquid-gas phase transition. These compounds are highly inert and non-toxic materials and have been successfully used in variety of biomedical applications including blood substitutes [30–35] and *in vivo* imaging [36,37].

We hypothesized that after conversion of a nanodroplet into a microbubble, the distinct interphase between aqueous surrounding and the PFC gas will provide a sharp, local refractive mismatch and therefore elicit THG. To demonstrate applicability of these nanodroplets in 3D settings, we applied infrared two-photon excitation of the embedded dye molecules to promote liquid to gas phase transition of PFC nanodroplets and recorded precise, spatiotemporally controlled nanodroplet activation. The results reveal a first-in-field phase-change nanodroplet system for spatially and temporally controlled and activatable probes for THG imaging.

Biomedical Optics EXPRESS

2. Materials and methods

2.1 Synthesis and assessment of nanodroplets

The nanodroplets were synthetized from a liquid dodecafluoropentane core coated by a mixture of phospholipids and Cyanine 3 (Cy3) dye molecules. The formulation was adopted from a previously described protocol [28]. Briefly, 1,2-distearoyl-sn-glycero-3-phosphocholine (DSPC), 1,2-distearoyl-sn-glycero-3-phosphoethanolamine-N-methoxy-polyethyleneglycol-2000 (DSPE-PEG-2000), and cholesterol (all from Avanti Polar Lipids, Inc.) were dissolved in 2 mL of chloroform at a weight ratio of 90:8.5:1.5, respectively, and the total mass of 20 mg. The mixture was dried in a rotary evaporator (Cole-Palmer Instrument Company, LLC.) at 40°C for 30 minutes to form a lipid cake. Then, 2 mL of deionized water was added to the lipid cake and the vial was shaken at 250 rpm on ice for 30 minutes. Simultaneously with the lipid hydration process, 125 µL of dodecafluoropentane (FluoroMed L.P.) was mixed with 100 µL of 1% (v/v) aqueous solution of 1H,1H,2H-Perfluoro-1-hexene,3,3,4,4,5,5,6,6,6-nonafluoro-1-hexene (Zonyl PFBE, Sigma-Aldrich Corp.) and 150 µL of 2 mg/mL aqueous solution of Cy3 dye (Lumiprobe Corp.). This core mix was vortexed for 20 seconds and then sonicated in a benchtop ultrasonic bath CPX-962-218R (Fisher Scientific) in ice-cold water for 30 seconds. Subsequently, 2 mL of rehydrated phospholipids were added to the core mixture of PFC, Cy3 dye, and Zonyl PFBE. The suspension was vortexed for 30 seconds and then sonicated in the benchtop ultrasonic bath in ice-cold water for 1 minute. Final sonication was carried out using the VCX 500 ultrasound probe with a 2 mm tip (Cole Palmer) for two 1 minute cycles at 25% maximum amplitude; the cycles were separated by 20 seconds of vortexing. Then, the suspension was kept on ice for 5 minutes and was washed twice with water at 3100 G for 15 minutes to remove the excess of free dye and lipids. The final pellet of washed nanodroplets was re-suspended in 1 mL of deionized water. Blank nanodroplets (containing no dye) were synthesized using the same protocol except deionized water was added to the core mix instead of the dye solution.

Average size of the nanodroplets was measured by dynamic light scattering using intensity (Delsa Nano C, Beckman Coulter, Inc.). To confirm dye inclusion inside the nanodroplets, fluorescence intensity of blank and dye-containing preparations were measured with Synergy HT microplate reader (BioTek Instruments, Inc.) using 530/25 and 590/35 nm excitation/emission filters.

PFC concentration in nanodroplet preparations was measured using ^{19}F NMR. Briefly, 10 µL of a nanodroplet suspension were mixed with 400 µL of deionized water, and 75 µL of 0.5% reference solution of trifluoroacetic acid in deuterium oxide (both from Sigma-Aldrich Corp.) in a 5 mm NMR sample tube (Wilmad-LabGlass). One-dimensional ^{19}F NMR was performed with a 500 MHz NMR spectrometer (Bruker Corporation). Typical acquisition parameters included acquisition time of 0.577 s, signal averages - 16 (with phase cycling) and a relaxation delay of 15 s. Spectral amplitudes were corrected for incomplete relaxation and fluorine quantification was carried out by integrating peaks and comparing the sample's peak to the reference peak from trifluoroacetic acid standard.

2.2 Phantom preparation

Polyacrylamide (10%, PAA) phantoms were made by adopting a previously described protocol [38]. Briefly, 125 µL of 40% acrylamide aqueous solution (Ambion Inc.), 7.5 µL of 438 mM aqueous solution of ammonium persulfate (Sigma-Aldrich Corp.), 0.75 mg of nanodroplets (in terms of PFC concentration, the corresponding volume was varied depending on a preparation but was typically 20-60 µL), 2 µL of tetramethyl ethylenediamine (Sigma-Aldrich Corp.), and deionized water to bring the final volume up to 500 µL were mixed together and poured inside of a 20 mm diameter and 2 mm high silicone isolator (Grace Bio-Labs) attached to a macroscopy slide. Isolators were sealed with a 24 x 24 mm cover glass

Biomedical Optics EXPRESS

(Fisher Scientific) and the mixture was allowed to polymerize to a 10% PAA gel at room temperature for 20 minutes before imaging.

2.3 Multiphoton microscopy imaging

Imaging was performed on a custom multiphoton microscope (TriMScope-II, LaVision BioTec), equipped with three tunable Ti:Sa (Coherent Ultra II Titanium:Sapphire) lasers and two Optical Parametric Oscillators (OPOs; Coherent APE). Power under the objective was controlled by attenuators in the beams paths and measured before each experiment. A long-working distance, 25x NA 1.05 water immersion objective (Olympus) was used for image acquisition. Multi-spectral detection was performed using up to 3 GaSP photomultipliers (PMTs, Hamamatsu) in the backward configuration using sequential single or dual excitation wavelengths scans for z-stack, zoom and overview, and time lapse acquisitions. The following excitation and emission channels were collected where indicated: Lifeact-GFP and calcein AM (920 nm; 525/50 nm); H2B-mcherry (1090 nm or 1100 nm; 620/60 nm), SHG (1090 nm; 525/50 nm), and THG (1280 nm; 420/50 nm). Nanodroplets were excited with 1090 nm or 1100 nm two-photon excitation (100-200 mW measured under the objective) and phase-change induced THG signals were detected using 1280 nm multi-photon excitation using 80-110 mW under objective in cell culture in vitro which is comparable for imaging in the mouse dermis *in vivo*. Time-lapse recordings were performed by acquiring images every 2 seconds for 200 to 400 seconds. The 1090 nm or 1100 nm wavelength for nanodroplet activation was applied for continuous intervals to generate THG signals. Single time point, 3D multichannel z-stacks were acquired with z step sizes of 3 µm. Scan fields had a pixel dwell time of 4 µs (imaging in ND suspensions) and 8.9 µs (imaging in gel phantoms and collagen matrix).

2.4 THG signal and image analysis

THG signal and image analysis was performed using Fiji/ImageJ2 [39], Excel (MS) and results were displayed with GraphPad Prism 7. To measure the dependence of signal generated by activated PFC nanodroplets on excitation power, Cy3 PFC nanodroplets were first excited using 1100 nm (~110 mW) in imaging media, phosphate buffered saline with Ca^{2+} and Mg^{2+} (Sigma-Aldrich Corp) and 10% fetal bovine serum (Cellgro) mixed with 20 µL of nanodroplets, and 1280 nm excitation (~90 mW) to obtain microbubble signal emission (420/50 nm). Once microbubbles were detected, photoactivation at 1090 nm was ceased and 1280 nm excitation over a range of available powers (89-186 m W) was used alone to collect single images from the induced microbubbles at a single focal plane. The mean intensity of 5 microbubbles from 4 independently excited positions in cell culture was quantified using MaxEntropy thresholding (Fiji). Signal-power data set were log-log transformed and individually fitted using a linear regression. The R^2 values for all 5 fits was > 0.97. The mean of the slopes ($slope_m$) determined from each data set was calculated and reported with the standard deviation ($slope_m = 2.92 \pm 0.53$). For display, all log-log transformed data sets were plotted together with a fit line (mean slope and y-intercept of the individually modeled data sets).

Quantification of THG signals induced at defined z positions (Fig. 4(a)) in PAA gels was performed by first measuring the raw integrated density (total intensity) of each z slice of the acquired 3D stack. Background signal was estimated by using the Yen threshold method in Fiji and measuring the raw integrated density (bkg-intensity) for the identified background area for each z slice. Final THG intensity (AU) was reported as the difference between the total intensity and the bkg-intensity as determined above and then plotted as a function of the z position (µm).

Size distribution of THG microbubbles formed in solution was estimated from time-lapse imaging data. Background intensity of time-lapse recordings was estimated by measuring the mean intensity of the first 25 images (where no nanodroplets were excited). All time-lapse

Biomedical Optics EXPRESS

images were background corrected with this value. THG signal was discriminated from background using the Moments threshold method in combination with particle analysis to identify THG positive events of at least 2 square pixels in dimension (~0.6 μm^2). The areas of all identified THG pixels were measured. Assuming that all THG microbubbles are spherical upon formation and appear circular during single focal plane detection, the measured areas were converted into an 'apparent' circular diameter for size distribution analysis.

2.5 Cell culture, collagen matrix embedding and viability test

Mouse mammary 4T1 carcinoma cells stably expressing nuclear (H2B-mCherry) and actin filament binding (Lifeact-GFP) fluorescent reporters were maintained at 37°C and 5% CO_2 in RPMI-1640 medium (Sigma-Aldrich Corp.) supplemented with 10% fetal bovine serum (Cellgro Corning), 100 U/mL penicillin and 100 µg/ml streptomycin (Hyclone ThermoFisher) and 1% sodium pyruvate (ThermoFisher). Cells were detached with EDTA (1mM) and trypsin (0.5%) and the collected cell suspensions were incorporated into type I collagen from rat-tail tendon (BD Biosciences; final concentration 2.5 mg/mL) followed by gel polymerization at room temperature as described previously [40,41]. Using either the same silicon isolator and setup as for the PAA phantoms or a 35 mm glass bottom µ-Dish (ibidi GmbH), polymerized cell-containing collagen matrix was overlaid with culture or imaging media (1-3 mL) mixed with 40-120 µL of PFC nanodroplets in water and imaged after 20-30 minutes.

Human HT1080 fibrosarcoma cells stably expressing nuclear (H2B-mCherry) and actin (Lifeact-GFP) fluorescent reports were maintained in DMEM medium (Gibco/ThermoFisher) and supplemented with 10% fetal bovine serum (Cellgro Corning), 100 U/mL penicillin and 100 µg/ml streptomycin. After detachment and embedding into 3D collagen gels, as described above, cells were treated with 4-10 µM calcein AM (Corning) for 15 min, washed, treated with 1 mL imaging media (method 2.4) mixed with 20-40 µL of ND-Cy3 nanodroplets as above, and cell viability was tested after nanodroplet activation.

3. Results and discussion

3.1 Nanodroplets characterization

The nanodroplets consisted of a liquid PFC core coated with a mixture of PEGylated phospholipids, and embedded Cy3 dye molecules (Fig. 1(a)). The phospholipid coating stabilizes PFC nanodroplets in an aqueous environment while PEG provides protection from nonspecific interactions and Cy3 chromophores with an absorbance maximum at 550 nm were embedded to enable two-photon absorption and photoactivation. Nanodroplet-containing aqueous solution displayed characteristic purple coloring when Cy3 dye was embedded (Fig. 1(b)). Typical preparations resulted in fairly uniform size distributions of nanodroplets with average sizes at the major distribution peak of 379 ± 96 nm and 306 ± 80 nm for PFC nanodroplets with embedded Cy3 chromophores (ND-Cy3) and "blank" PFC nanodroplets without dye molecules (ND-B) specimen, respectively (Fig. 1(c)). Fluorescence intensity measurements confirmed dye inclusion inside the ND-Cy3 nanodroplets (Fig. 1(d)).

Biomedical Optics EXPRESS

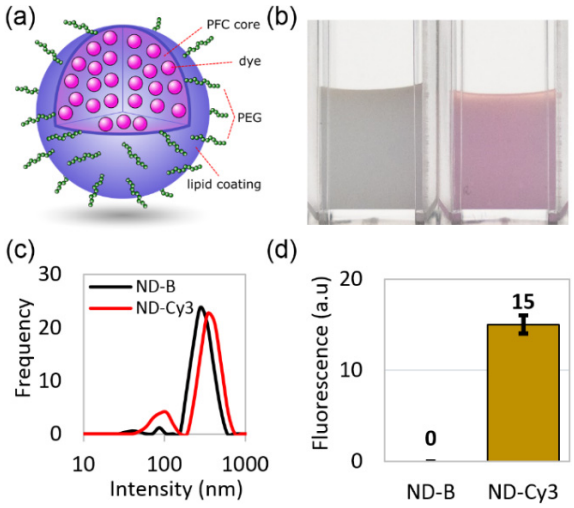

Fig. 1. (a) Schematic of a nanodroplet with lipid coating and PFC core containing dye molecules (ND-Cy3); (b) a photograph of washed preparations of "blank" nanodroplets with no dye (ND-B, left) and ND-Cy3 (right); (c) size distributions of nanodroplets measured by dynamic light scattering (intensity distribution); (d) difference in fluorescence between washed ND-B and ND-Cy3 nanodroplets at the same concentrations.

3.2 Two-photon activation of PFC phase-change nanodroplets

The nanodroplets were designed to enable an externally triggered phase-change by incorporating a visible dye to absorb incoming NIR photons through a two-photon absorption process. The choice of the perfluoropentane as the core material was driven by its relatively low boiling temperature of 29°C in bulk. It is important to note, that the boiling temperature is inversely proportional to nanodroplet size due to increase in the surface tension [42–44]. We hypothesized that two-photon excitation would induce a liquid-gas phase change of the PFC core through the highly localized heating created by the embedded chromophores resulting in an interface between aqueous surroundings and the PFC microbubble that can be detected by THG microscopy.

To confirm this hypothesis, we activated ND-Cy3 with 1100 nm two-photon laser excitation (or 1090 nm) tailored to the predicted two-photon absorption peak of Cy3. Previously, it was shown that two-photon fluorescence of Cy3 labeled IgG immunoglobulins can be excited in the range of ~930-1150 nm with the maximum two-photon fluorescence at 1032 nm [45]; this data indicate that the optimum two-photon absorption peak of Cy3 might differ from the predicted value. However, our two-photon imaging system did not have sufficient power at wavelengths below 1080 nm for nanodroplet activation, therefore, we used the 1100 nm excitation. Any THG signals resulting from the phase transition were excited using a higher infrared wavelength (1280 nm), which does not excite Cy3 dye, and detected at 395-445 nm, which is below the Cy3 emission.

Each nanodroplet preparation with or without the dye was embed in 10% PAA phantoms. All samples were continuously imaged (image acquired every 2 seconds) with a 1280 nm laser for the duration of the experiments (200 to 400 seconds) in order to detect any phase-change signals (Fig. 2(a) schematic). We first confirmed that continuous 1280 nm excitation alone over a period of 50 seconds did not elicit any signals in ND-Cy3 samples (Fig. 2(b)). Addition of the Cy3 excitation laser (1100 nm) resulted in formation of phase-change signals in the THG emission channel (Fig. 2(c)). After discontinuation of 1100 nm excitation, the phase-transition signal originating from microbubbles persisted for at least 50 sec (Fig. 2(d)). In contrast, little to no signal was induced when 1100 nm excitation was applied to dye-free ND-B blank nanodroplets for extended time periods (350 sec) (Figs. 2(e)–2(g)). A small

Biomedical Optics EXPRESS

number of sporadic phase-transition signals observed in some ND-B samples after a long observation period are most likely due to spontaneous phase change in some of the bigger and thus less stable PFC nanodroplets (Fig. 2(g), arrowhead).

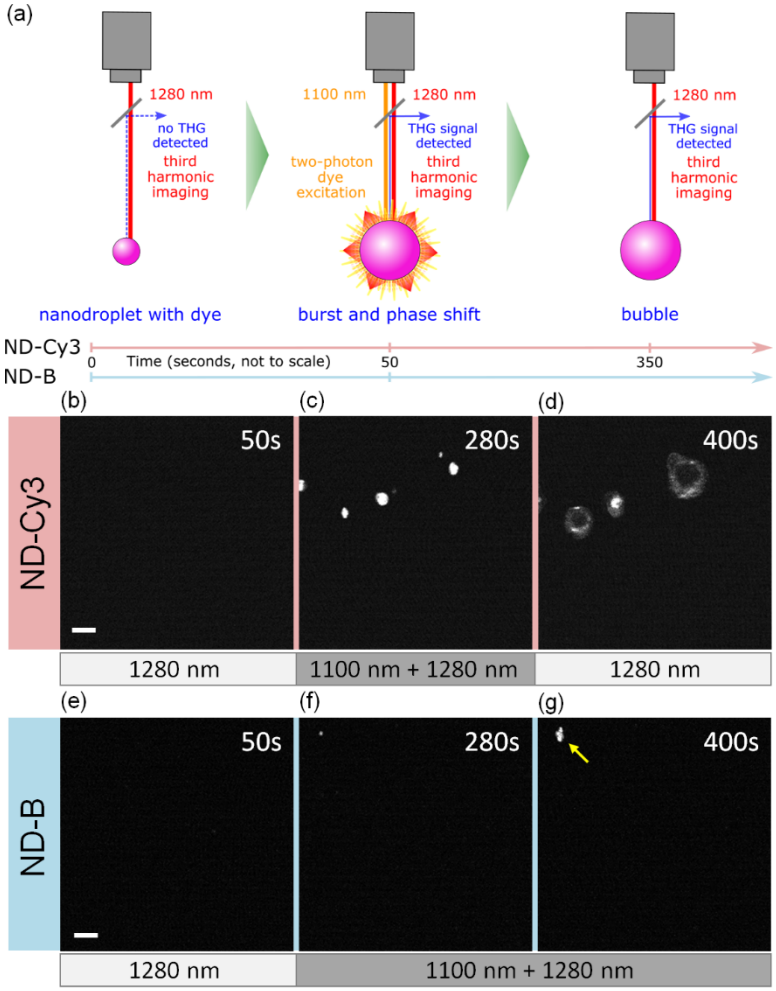

Fig. 2. Phase-change of nanodroplets with applied two-photon excitation. (a) Schematic of the experiment. Note, that both laser beams were delivered through the same objective. Single focal planes in gels with embedded ND-Cy3 (b, c, d) and ND-B (e, f, g) were continuously imaged with 1280 nm excitation for phase-change signal detection. No signal was registered in ND-Cy3 sample before 1100 nm excitation that was started after 50 seconds (b). Phase-change signal was registered during (c) 1100 nm laser excitation and (d) after its removal at 350 seconds. A similar sequence with extended 1100 nm excitation showed minimal signals for ND-B (e) before, and (f, g) during 1100 nm laser excitation starting after 50 and ending at 400 seconds; an arrowhead points to a rare, sporadic event. Scale bars = 10 µm.

In general, the liquid-gas phase transition is expected to result in up to ~5-6 fold volume increase based on the difference in density between gaseous and liquid phases of PFC [42,46]. However, previous studies of ultrasound activated PFC phase transition from nano- or micro-droplets to microbubbles showed a volume increases in excess of 10-fold [42,46–49]. The extra bubble expansion was shown to be associated with diffusion of dissolved gases from the surrounding media into the activated microbubbles due to an order of magnitude higher solubility of some gases in perfluorocarbon in comparison to water [50]. Consistently, PFC nanodroplets, with an average initial size just under 400 nm, reached sizes of ~4 µm in

Biomedical Optics EXPRESS

diameter after laser activation and transition to bubble state (Fig. 2(c)). However, occasionally after removal of the 1100 nm excitation, PFC microbubbles underwent further growth to diameters beyond 10 µm (Fig. 2(d)). This phenomenon was observed and extensively studied by the ultrasound imaging community with observed continuous growth over a period of minutes post liquid-gas phase change [44,49,51,52]. A number of mechanisms were proposed including coalescence of bubbles and/or bubbles with droplets to form larger secondary bubbles [51,53] and the Oswald ripening effect, by which dissolved air or gaseous PFC diffuses from smaller primary bubbles into larger secondary bubbles [49,53,54]. The Oswald ripening effect may be predominant in a gel environment where movement of primary formed microbubbles is restricted.

Overall, our data showed that two-photon excitation of ND-Cy3 within the predicted two-photon absorption peak of Cy3 results in efficient triggering of nanodroplet phase-change and subsequent microbubble formation detected in a THG region (395-445 nm). This illustrates the proof of principle that such nanodroplets can be used as inducible phase-change probes for multiphoton imaging.

3.3 Power dependence of the phase-change signal

To confirm that the phase change signal generated by the activated PFC nanodroplets was indeed THG, we activated ND-Cy3 nanodroplets in an aqueous suspension (compatible with cell culture) with 1100 nm (~110 mW) and simultaneously monitored microbubble formation using 1280 nm excitation (~90 mW) and detection with 395-445 nm filter. Once microbubble were detected, 1100 nm excitation was terminated and 1280 nm excitation was retained after which the dependence of intensity of the signal generated by the microbubbles on excitation power was obtained. The log-log transformation of each signal-power dependence data set was fit using linear regression with all fits having $R^2 > 0.97$ (Fig. 3). The mean ± standard deviation of the obtained slopes was 2.92 ± 0.52 indicating that the signal generated by the activated microbubbles is a 3rd order process. Taking into account that the signal was detected at the triple frequency of the excitation wavelength, our data indicate that the microbubbles produce a THG signal.

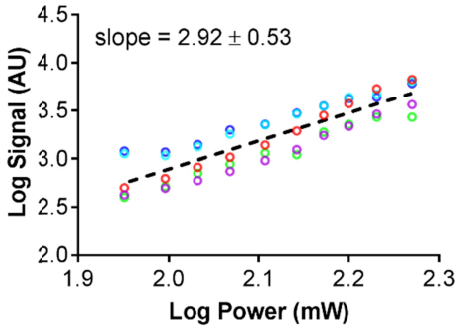

Fig. 3. PFC nanodroplets phase-change signals are a THG process. Single focal plane images of n = 5 microbubbles were collected using 1280 nm excitation over a range of laser powers (89-186 mW). Log-log transformed signal-power data sets (colored circles, n = 5) from 5 microbubbles at 4 independent positions are plotted with a fit line (dashed line) that represents the means of slopes and y-intercepts obtained from linear regressions of each of the five data sets. The mean slope of ~3 indicates a third order process.

3.4 Spatial control of nanodroplets activation

Next, we investigated whether two-photon excitation can be used to selectively activate nanodroplets at different focal positions in depth along the z-axis of our phantoms. For this experiment we prepared phantoms with distributed ND-Cy3 nanodroplets. Three different

Biomedical Optics EXPRESS

focal planes separated by 50 µm in depth were sequentially excited with a two-photon 1090 nm laser starting from the deepest focal plane and moving towards the surface (Fig. 4(a), left). During nanodroplet activation, simultaneous excitation at 1280 nm using an independent OPO was used to concurrently detect THG events. After completing the activation process in the three separate focal plans, a z-scan comprising the excited planes was acquired for THG detection using only 1280 nm excitation. The lateral projection of this 3D scan clearly shows localized THG signal from activated ND-Cy3 nanodroplets in the three focal planes where 1090 nm excitation was used, confirming that two-photon excitation resulted in a spatially controlled nanodroplet phase-change (Fig. 4(a), right and Visualization 1). Indeed, quantification of the THG signal as a function of depth further confirmed the focal nature of ND-Cy3 activation (Fig. 4(b)). The decreasing THG signal from the upper to lower activated layers is likely consequence of decreasing effective intensity and dye activation by the 1100 nm incident laser with increasing tissue penetration and light scatter.

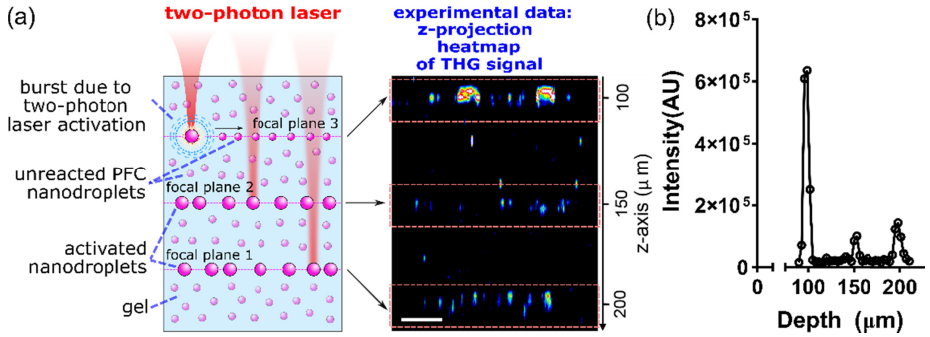

Fig. 4. (a) ND-Cy3 nanodroplets embedded in a PAA gel phantom were excited in three focal planes at various depths starting from the deeper layer and moving upwards (left: experimental design). Experimental data from z-projection of 3D stack containing THG signals in the gel volume showed three separate focal planes with ND-Cy3 THG signals (right). Scale bar, 20 µm. (b) Integrated intensity measurements of THG signals as a function of z-depth into the PAA gel from the coverglass (z = 0 µm) confirm the focal nature of THG signal.

3.5 Temporally controlled activation of nanodroplets in suspension

After establishing that dye-loaded PFC nanodroplets can be spatially activated in a 3D gel, we wanted to further characterize the temporal control of the phase-changes in an aqueous suspension of ND-Cy3. A suspension of ND-Cy3 in water was used for these experiments and illuminated at a single focal plane. Similar to NDs in the PAA phantom, no THG signal was detected during 1280 nm excitation alone (up to 50 sec continuous exposure) (Fig. 5(a)), suggesting high particle stability under THG monitoring conditions. Upon addition of the 1090 nm excitation, dynamic THG events (Figs. 5(b), 5(c), and Visualization 2) were observed. Once the 1090 nm excitation source was removed (at 150 seconds), the THG signal returned to zero as PFC microbubbles, which were freely moving within the aqueous environment, redistributed out of the imaging plane (Fig. 5(d)). These data show that ND-Cy3 activation can be temporally controlled. The vast majority of activated microbubbles in the solution where smaller or approaching ~4 µm size when detected by THG (Fig. 5(e)). As discussed above, microbubbles with sizes up to ~4 µm are expected after droplet-bubble phase transition of ~400 nm diameter PFC nanodroplets. As can be seen in Visualization 2, microbubbles activated in solution quickly leave the focal plane due to buoyancy that makes it less likely for them to develop larger secondary bubbles observed in gel phantoms above (Fig. 2(d)). Therefore, the experiments in solution are more likely to reflect the initial size of the microbubbles right after laser activation of the droplets.

Biomedical Optics EXPRESS

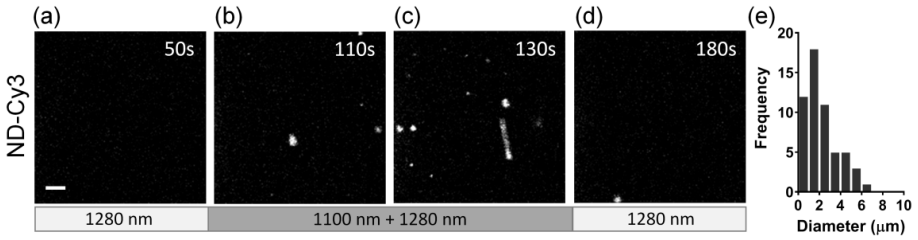

Fig. 5. THG detection of PFC phase-change during 2-photon excitation of a ND-Cy3 suspension. (a) A small region (44x44 μm) in a water solution of ND-Cy3 nanodroplets was subjected to continuous (0-200 seconds) excitation with 1280 nm for detecting THG signals and after 50 seconds dually excited with activating 1090 nm laser (~168mW). THG signals were observed forming over time under dual excitation (b, c) and then the THG signal disappeared once 1090 nm excitation was removed at 150 seconds (d). Imaging concluded at 200 s. Scale bar = 5 μm (e) Size distribution of the THG signals over duration of the experiment.

3.6 Activation of nanodroplets in 3D cell culture

For preliminary validation of the potential utility of dye-loaded PFC nanodroplets in biological studies, we generated 3D collagen matrix with embeded 4T1 mouse breast cancer cells expressing nuclear H2B-mCherry and Lifeact-GFP detecting actin filaments [55]. Culture media mixed with ND-Cy3 was incubated with the 3D cell culture before multiphoton imaging. Similar to our method of imaging phantom and suspension samples, 3D cell cultures were initially imaged using 1280 nm laser excitation (0-52 seconds) to confirm the absence of non-specific induction of THG (Fig. 6(a)) followed by additional exposure to 1090 nm excitation for nanodroplet activation (during 52-100 seconds in the imaging sequence). We observed time dependent activation of the nanodroplets, with the emerging THG signals adjacent to the cells between 52 to 100 seconds of 1090 nm excitation (Fig. 6(b) and Visualization 3). Most of the microbubbles appear to form extracellularly (see arrows in Figs. 6(b) and 6(c)), although, we cannot exclude the possibility of some nanodroplets been also endocytosed by cells. As in the case of PAA phantoms, the initially formed microbubbles underwent a significant size expanson over time after 100 seconds despite removal of the 1090 nm laser (Figs. 6(c)–6(f) and Visualization 3). There were apparent coalescence events contributing to growth of the microbubbles (Figs. 6(d)–6(f) and Visualization 3). Differences in the expansion of microbubbles are most likely asociated with local non-uniformity of nanodropet distribution in the cell culture as well as non-uniformities in activation of liquid-gas phase transition of PFC nanodroplets due to differences in their dye loading and sizes. The microbubbles with bigger initial sizes can undergo faster growth due to the Oswald ripening effect and coalescence of bubbles and/or bubbles with droplets as described in Section 3.2. THG signals were confined to the activated area demonstrating controlled spatial activation (Fig. 6(g)). Fate-tracing of activated nanodroplets indicates interactions with cell surfaces and potentially integration of the plasma membrane of the adjacent cells into coating of the growing microbubbles (Figs. 6(d)–6(f) and Visualization 3).

Notably, the mCherry signal inside the activated area was diminished after exposure to photoactivation, suggestive of photobleaching (Fig. 6(g), dashed box). To test this assumption we carried out an experiment where mCherry expressing cells were labeled with calcein AM vital dye and were exposed to 1090 nm laser at 102 mW for 150 seconds to mimick conditions of nanodroplet activation used in our studies (data not shown). A continuous decay in the mCherry signal was observed with no decay in the calcein AM fluorescence indicating photobleaching of mCherry label whithout photo-cytotoxicity.

Biomedical Optics EXPRESS

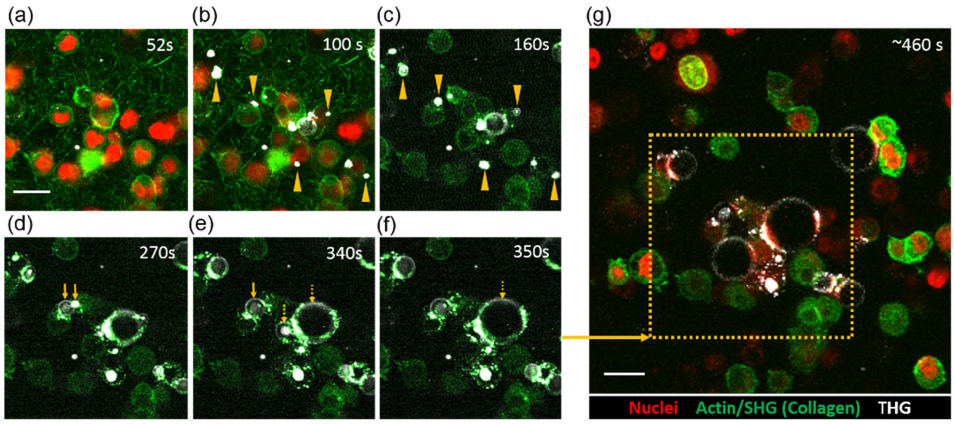

Fig. 6. ND-Cy3 nanodroplets excited in 3D collagen matrix with cancer cells. Laser sequence: 52-100 seconds 1090 nm and 1280 nm; 102-400 seconds 1280 nm; 460 seconds overview snapshot 1090 nm and 1280 nm. (a) Single focal plane of 4T1 murine breast cancer cells dispersed in collagen I matrix at the start of start of two-photon (1090 nm) excitation (t = 52 seconds). THG and GFP-Lifeact/actin signals are detected by continuous 1280 nm excitation (0-400 seconds) while collagen and cell nuclei are detected by 1090 nm during excitation of nanodroplets (see Methods). (b) During ~50 seconds of 1090 nm excitation, THG events are observed forming near cells (examples are marked by arrowheads in b and in c). Post-activation, THG microbubbles evolve (c-f) and expand into cells. Continuous imaging shows examples of small (d, e – solid arrows) and large (e, f – dashed arrows) microbubbles coalescence into larger microbubbles. (g) Overview using 920 nm (actin), 1090 nm (at reduced power; nuclei only), and 1280 nm (THG) ~6 minutes post ND-Cy3 activation of the defined area (dashed box) shows spatially induced THG microbubbles; note that the nuclear mCherry signal was photobleached, however cell morphology remained intact. Scale bars = 20 µm.

To further investigate the impact of activated microbubbles on cell integrity, we embedded human HT1080 fibrosarcoma cells (a mesenchymal cell type) stably expressing H2B-mCherry (nuclei) and LifeAct-GFP (actin) into 3D collagen matrix. Cells were loaded with calcein AM, a vital dye that allows to assess the integrity of the cell membrane as a measure for cell viability. Cytoplasmic calcein AM signal was clearly detectable on the background of LifeAct-GFP (Fig. 7(e)). Dye-loaded PFC nanodroplets were topically applied to the sample. Pre-nanodroplet activation, cells showed strong calcein AM signal in their cytoplasm, indicative of an intact plasma membrane (Fig. 7(a)). Liquid-gas phase change of the nanodroplets was activated with 1100 nm for 78 seconds under continuous monitoring of THG using excitation at 1280 nm. Subsequently, the calcein AM and THG signals were monitored with 920 nm and 1280 nm, respectively. In an example in Fig. 7(b) microbubbles were formed in vicinity of cells 1 and 3. The growing microbubble in contact with cell 1 appeared to integrate with the cell plasma membrane (Fig. 7(c)), and thus was followed by loss of calcein AM signal (Fig. 7(d)), indicative of the cell death. Similarly, expansion of the microbubble proximal to cell 3 led to loss of calcein AM signal (Figs. 7(c) and 7(d)). Cell 2 that was in close vicinity to the formed microbubbles without a direct mechanical contact remained unperturbed (Figs. 7(b)–7(d)). Of note, despite imaging for up to 60 minutes, the calcein AM signal in cell 2 did not fade, indicating prolonged viability.

Our data demonstrate that activated microbubbles can cause mechanical stress to proximal cells through pushing, cell displacement, and disruption of cell membranes. Clearly, more studies are needed to fully realize the potential of our nanodroplets as agents for spatiotemporaly controlled delivery and activatable THG agents, but these early experiments show promise that such applications are within reach.

Biomedical Optics EXPRESS

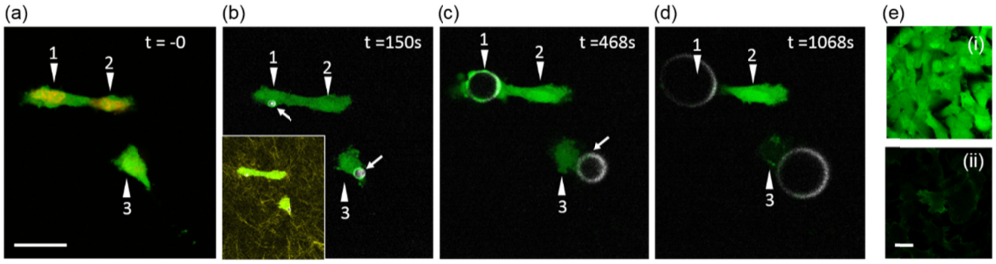

Fig. 7. Impact of microbubble interactions with cells. Laser sequence: t = 0 snapshot 920 nm (calcein AM) and 1100 nm (mCherry); 0-50 seconds 1280 nm (THG and calcein AM); 52-132 seconds 1100 nm (activation of PFC nanodroplets) and 1280 nm (THG and calcein AM); 920 nm and 1280 nm for all other times. (a) HT1080 cells (numbered arrows) expressing H2B-mCherry and Lifeact-GFP pre-labeled with vital dye calcein AM in a collagen matrix before activation of ND-Cy3 nanodroplets. (b) Microbubble formation is visible as white spots proximal to cells 1 and 3 following activation of nanodroplets with 1100 nm (~128 mW). THG and calcein AM signals were monitored using 1280 nm and 920 nm, respectively, every 1 minute for up to 60 minutes. Inset shows all 3 cells in collagen matrix. (c and d) Mechanical perturbation of cells 1 and 3 by expanding microbubbles post activation. (e) Control showing calcein AM signal (i) dominates endogenous HT1080 Lifeact-GFP (ii) signal (~7 mW 920 nm). Scale bar = 25μm.

4. Conclusions and perspective

Here we describe a new class of activatable agents for THG that are based on dye-loaded phase-change PFC nanodroplets. The agents respond to two-photon laser light excitation of the nanodroplet-embedded dye molecules, expand, and generate strong THG contrast. This activation process occurs in a spatially and temporally controlled manner that offers exciting possibilities of applying these nanoparticles as nanocarriers for delivery of a cargo 'on-demand' using two-photon excitation under THG monitoring. Various compounds, like drugs or biologically active agents, could be incorporated inside the nanodroplets akin to the dye molecules used in this study [44,56,57]. We further envision applying variants of these nanodroplets toward labeling cells and extracellular matrix specific proteins and for identifying niches of enzymatic/metabolic activity. Such pairing of nonlinear optical microscopy and novel THG agents has the potential to provide new insights into both basic cellular functions (malfunctions) and diagnostic medicine.

The range of 100-200 mW for two-photon excitation of the nanoparticles is relatively high as the typical time-lapse imaging with two-photon excitation is carried out using power between 5 and 130 mW [13,55,58–60]. Photodamage is a function of excitation wavelength and power, the period of observation, instantaneous and cumulative illumination relative to the observation period, and absorption/scatter of the incident light by the tissue. Therefore, despite high nominal excitation power, photodamage caused by infrared excitation (1090 to 1280 nm) *in vivo* is acceptable at a high power of 130 mW with short scan time per frame (~1 frame per second) for over 230 frames taken over 3.8 hours [8,13]. However, tissue photodamage is observed at a slower rate of 0.6 frame per second under continuous scanning, without intervals [13]. Currently, we are able to excite the nanodroplets in our cell culture experiments at powers of 115-134 mW at a rate of 0.73 frames per sec and exposure for 40 frames (~80 seconds total exposure). These excitation parameters are just above the imaging condition that can cause adverse effects in biological samples when continuously applied. Accordingly, this cumulative exposure was not cytotoxic to cells with follow-up imaging up to 60 minutes, using vital staining with calcein AM. We are working on increasing dye loading efficiency into the PFC nanodroplets in order to significantly reduce the power required to induce the liquid-gas phase transition. One promising direction is synthetizing perfluorocarbon-soluble chromophores [61–64]; these modified dyes can be solubilized inside the perfluorocarbon core that could permit significantly decreased power for initiating the

Biomedical Optics EXPRESS

liquid-phase transition. The THG excitation (80-100 mW) used for time-lapse detection of microbubble growth is comparable to THG imaging of cells in other studies *in vitro* and *in vivo* [12,13,65,66].

The effects of microbubble expansion on cell viability in direct vicinity may pose challenges in tissue imaging applications, but also open avenues for other applications. To control cell damage, we currently focus on minimizing the expansion of activated microbubbles starting with achieving a more uniform distribution of nanodroplets in cell cultures and optimizing nanodroplet concentration. For interventional purposes, we envision, for example, increasing permeation of blood vessels, e.g. in blood-brain barrier, via precise disruption of endothelium under THG monitoring. A similar concept was recently reported using microbubble-assisted focused ultrasound [67]. We thus foresee that the spatial precision of two-photon-mediated delivery as a tool in pre-clinical studies may offer particular opportunities for localized delivery. Likewise, locally triggered disruption of cancer cells may be exploited for release of cancer antigens for immunotherapy [68,69]. Finally, due to high level of interest in applications of PFC nanodroplets in photoacoustic and ultrasound imaging [38,70–72], it is important to have tools that would allow a high resolution longitudinal imaging of PFC nanodroplet activation in biological samples similar to our study presented here.

Potential applications of the two-photon activatable phase-change nanodroplets could be greatly facilitated by the pioneering work of Professor Tuchin in the area of tissue optical clearing (TOC) [73–77]. This method is based on modifying refractive index of biological tissues that leads to reduction of tissue light scattering and making biological specimen more transparent [78]. The combination of multiphoton microscopy and TOC was shown to achieve depth of penetration in biological tissues exceeding 1000-2000 μm [79,80]. Therefore, application of TOC could significantly increase the depth in tissue where presented here activatable THG agents can be excited and imaged, thus extending the range of their potential applications.

Funding

National Institutes of Health (NIH)/National Cancer Institute (NCI) (R21 CA231561, P30 CA016672); Genitourinary Cancers Program of the CCSG shared resources at The University of Texas MD Anderson Cancer Center; Prostate Cancer Moonshot Program at The University of Texas MD Anderson Cancer Center; the European Research Council (617430-DEEPINSIGHT); the NIH (U54 CA210184-01); and the Cancer Genomics Center (CGC.nl).

Disclosures

The authors declare that there are no conflicts of interest related to this article.

References

1. R. N. Germain, E. A. Robey, and M. D. Cahalan, "A decade of imaging cellular motility and interaction dynamics in the immune system," Science **336**(6089), 1676–1681 (2012).
2. K. Wolf and P. Friedl, "Functional imaging of pericellular proteolysis in cancer cell invasion," Biochimie **87**(3-4), 315–320 (2005).
3. J. A. Thomas, "Optical imaging probes for biomolecules: an introductory perspective," Chem. Soc. Rev. **44**(14), 4494–4500 (2015).
4. C. Martelli, A. Lo Dico, C. Diceglie, G. Lucignani, and L. Ottobrini, "Optical imaging probes in oncology," Oncotarget **7**(30), 48753–48787 (2016).
5. J. Condeelis and R. Weissleder, "In vivo imaging in cancer," Cold Spring Harb. Perspect. Biol. **2**(12), a003848 (2010).
6. F. Helmchen and W. Denk, "Deep tissue two-photon microscopy," Nat. Methods **2**(12), 932–940 (2005).
7. N. G. Horton, K. Wang, D. Kobat, C. G. Clark, F. W. Wise, C. B. Schaffer, and C. Xu, "In vivo three-photon microscopy of subcortical structures within an intact mouse brain," Nat. Photonics **7**(3), 205–209 (2013).
8. V. Andresen, S. Alexander, W. M. Heupel, M. Hirschberg, R. M. Hoffman, and P. Friedl, "Infrared multiphoton microscopy: subcellular-resolved deep tissue imaging," Curr. Opin. Biotechnol. **20**(1), 54–62 (2009).

Biomedical Optics EXPRESS

9. G. Kaushik, D. A. Gil, E. Torr, E. S. Berge, C. Soref, P. Uhl, G. Fontana, J. Antosiewicz-Bourget, C. Edington, M. P. Schwartz, L. G. Griffith, J. A. Thomson, M. C. Skala, W. T. Daly, and W. L. Murphy, "Quantitative Label-Free Imaging of 3D Vascular Networks Self-Assembled in Synthetic Hydrogels," Adv. Healthc. Mater. **8**(2), e1801186 (2019).
10. P. Sarder, S. Yazdanfar, W. J. Akers, R. Tang, G. P. Sudlow, C. Egbulefu, and S. Achilefu, "All-near-infrared multiphoton microscopy interrogates intact tissues at deeper imaging depths than conventional single- and two-photon near-infrared excitation microscopes," J. Biomed. Opt. **18**(10), 106012 (2013).
11. A. J. Walsh, R. S. Cook, J. H. Lee, C. L. Arteaga, and M. C. Skala, "Collagen density and alignment in responsive and resistant trastuzumab-treated breast cancer xenografts," J. Biomed. Opt. **20**(2), 026004 (2015).
12. B. Weigelin, G. J. Bakker, and P. Friedl, "Third harmonic generation microscopy of cells and tissue organization," J. Cell Sci. **129**(2), 245–255 (2016).
13. B. Weigelin, G. J. Bakker, and P. Friedl, "Intravital third harmonic generation microscopy of collective melanoma cell invasion: Principles of interface guidance and microvesicle dynamics," Intravital **1**(1), 32–43 (2012).
14. C. F. Chang, C. Y. Chen, F. H. Chang, S. P. Tai, C. Y. Chen, C. H. Yu, Y. B. Tseng, T. H. Tsai, I. S. Liu, W. F. Su, and C. K. Sun, "Cell tracking and detection of molecular expression in live cells using lipid-enclosed CdSe quantum dots as contrast agents for epi-third harmonic generation microscopy," Opt. Express **16**(13), 9534–9548 (2008).
15. K. Harpel, R. D. Baker, B. Amirsolaimani, S. Mehravar, J. Vagner, T. O. Matsunaga, B. Banerjee, and K. Kieu, "Imaging of targeted lipid microbubbles to detect cancer cells using third harmonic generation microscopy," Biomed. Opt. Express **7**(7), 2849–2860 (2016).
16. M. R. Tsai, C. Y. Lin, Y. H. Liao, and C. K. Sun, "Applying tattoo dye as a third-harmonic generation contrast agent for in vivo optical virtual biopsy of human skin," J. Biomed. Opt. **18**(2), 026012 (2013).
17. L. Cui, D. Tokarz, R. Cisek, K. K. Ng, F. Wang, J. Chen, V. Barzda, and G. Zheng, "Organized Aggregation of Porphyrins in Lipid Bilayers for Third Harmonic Generation Microscopy," Angew. Chem. Int. Ed. Engl. **54**(47), 13928–13932 (2015).
18. L. Dubreil, I. Leroux, M. Ledevin, C. Schleder, L. Lagalice, C. Lovo, R. Fleurisson, S. Passemard, V. Kilin, S. Gerber-Lemaire, M. A. Colle, L. Bonacina, and K. Rouger, "Multi-harmonic Imaging in the Second Near-Infrared Window of Nanoparticle-Labeled Stem Cells as a Monitoring Tool in Tissue Depth," ACS Nano **11**(7), 6672–6681 (2017).
19. S. Dietzel, S. Hermann, Y. Kugel, S. Sellner, B. Uhl, S. Hirn, F. Krombach, and M. Rehberg, "Multiphoton Microscopy of Nonfluorescent Nanoparticles In Vitro and In Vivo," Small **12**(24), 3245–3257 (2016).
20. K. A. Lukyanov, D. M. Chudakov, S. Lukyanov, and V. V. Verkhusha, "Innovation: Photoactivatable fluorescent proteins," Nat. Rev. Mol. Cell Biol. **6**(11), 885–890 (2005).
21. R. Ando, H. Hama, M. Yamamoto-Hino, H. Mizuno, and A. Miyawaki, "An optical marker based on the UV-induced green-to-red photoconversion of a fluorescent protein," Proc. Natl. Acad. Sci. U.S.A. **99**(20), 12651–12656 (2002).
22. G. H. Patterson and J. Lippincott-Schwartz, "A photoactivatable GFP for selective photolabeling of proteins and cells," Science **297**(5588), 1873–1877 (2002).
23. R. C. Gilson, R. Tang, A. Som, C. Klajer, P. Sarder, G. P. Sudlow, W. J. Akers, and S. Achilefu, "Protonation and Trapping of a Small pH-Sensitive Near-Infrared Fluorescent Molecule in the Acidic Tumor Environment Delineate Diverse Tumors in Vivo," Mol. Pharm. **12**(12), 4237–4246 (2015).
24. U. Chitgupi, S. Shao, K. A. Carter, W. C. Huang, and J. F. Lovell, "Multicolor Liposome Mixtures for Selective and Selectable Cargo Release," Nano Lett. **18**(2), 1331–1336 (2018).
25. A. Hannah, G. Luke, K. Wilson, K. Homan, and S. Emelianov, "Indocyanine green-loaded photoacoustic nanodroplets: dual contrast nanoconstructs for enhanced photoacoustic and ultrasound imaging," ACS Nano **8**(1), 250–259 (2014).
26. K. Wilson, K. Homan, and S. Emelianov, "Biomedical photoacoustics beyond thermal expansion using triggered nanodroplet vaporization for contrast-enhanced imaging," Nat. Commun. **3**(1), 618 (2012).
27. G. P. Luke, A. S. Hannah, and S. Y. Emelianov, "Super-Resolution Ultrasound Imaging in Vivo with Transient Laser-Activated Nanodroplets," Nano Lett. **16**(4), 2556–2559 (2016).
28. C. H. Liu, D. Nevozhay, A. Schill, M. Singh, S. Das, A. Nair, Z. Han, S. Aglyamov, K. V. Larin, and K. V. Sokolov, "Nanobomb optical coherence elastography," Opt. Lett. **43**(9), 2006–2009 (2018).
29. C. H. Liu, D. Nevozhay, H. Zhang, S. Das, A. Schill, M. Singh, S. Aglyamov, K. V. Sokolov, and K. V. Larin, "Longitudinal elastic wave imaging using nanobomb optical coherence elastography," Opt Lett. in press (2019).
30. K. C. Lowe, "Perfluorochemical respiratory gas carriers: applications in medicine and biotechnology," Sci. Prog. **80**(Pt 2), 169–193 (1997).
31. G. P. Biro, P. Blais, and A. L. Rosen, "Perfluorocarbon blood substitutes," Crit. Rev. Oncol. Hematol. **6**(4), 311–374 (1987).
32. N. M. Dietz, M. J. Joyner, and M. A. Warner, "Blood substitutes: fluids, drugs, or miracle solutions?" Anesth. Analg. **82**(2), 390–405 (1996).
33. S. F. Flaim, "Pharmacokinetics and Side Effects of Perfluorocarbon-Based Blood Substitutes," Artif. Cells Blood Substit. Immobil. Biotechnol. **22**(4), 1043–1054 (1994).

Biomedical Optics EXPRESS

34. P. A. Dayton, S. Zhao, S. H. Bloch, P. Schumann, K. Penrose, T. O. Matsunaga, R. Zutshi, A. Doinikov, and K. W. Ferrara, "Application of ultrasound to selectively localize nanodroplets for targeted imaging and therapy," Mol. Imaging **5**(3), 160–174 (2006).
35. R. F. Mattrey, "Perfluorooctylbromide: a new contrast agent for CT, sonography, and MR imaging," AJR Am. J. Roentgenol. **152**(2), 247–252 (1989).
36. E. T. Ahrens, R. Flores, H. Xu, and P. A. Morel, "In vivo imaging platform for tracking immunotherapeutic cells," Nat. Biotechnol. **23**(8), 983–987 (2005).
37. E. T. Ahrens, B. M. Helfer, C. F. O'Hanlon, and C. Schirda, "Clinical cell therapy imaging using a perfluorocarbon tracer and fluorine-19 MRI," Magn. Reson. Med. **72**(6), 1696–1701 (2014).
38. A. S. Hannah, G. P. Luke, and S. Y. Emelianov, "Blinking Phase-Change Nanocapsules Enable Background-Free Ultrasound Imaging," Theranostics **6**(11), 1866–1876 (2016).
39. C. T. Rueden, J. Schindelin, M. C. Hiner, B. E. DeZonia, A. E. Walter, E. T. Arena, and K. W. Eliceiri, "ImageJ2: ImageJ for the next generation of scientific image data," BMC Bioinformatics **18**(1), 529 (2017).
40. K. Wolf, M. Te Lindert, M. Krause, S. Alexander, J. Te Riet, A. L. Willis, R. M. Hoffman, C. G. Figdor, S. J. Weiss, and P. Friedl, "Physical limits of cell migration: control by ECM space and nuclear deformation and tuning by proteolysis and traction force," J. Cell Biol. **201**(7), 1069–1084 (2013).
41. K. Wolf, S. Alexander, V. Schacht, L. M. Coussens, U. H. von Andrian, J. van Rheenen, E. Deryugina, and P. Friedl, "Collagen-based cell migration models in vitro and in vivo," Semin. Cell Dev. Biol. **20**(8), 931–941 (2009).
42. P. S. Sheeran, V. P. Wong, S. Luois, R. J. McFarland, W. D. Ross, S. Feingold, T. O. Matsunaga, and P. A. Dayton, "Decafluorobutane as a phase-change contrast agent for low-energy extravascular ultrasonic imaging," Ultrasound Med. Biol. **37**(9), 1518–1530 (2011).
43. P. S. Sheeran, S. H. Luois, L. B. Mullin, T. O. Matsunaga, and P. A. Dayton, "Design of ultrasonically-activatable nanoparticles using low boiling point perfluorocarbons," Biomaterials **33**(11), 3262–3269 (2012).
44. N. Y. Rapoport, A. M. Kennedy, J. E. Shea, C. L. Scaife, and K. H. Nam, "Controlled and targeted tumor chemotherapy by ultrasound-activated nanoemulsions/microbubbles," J. Control. Release **138**(3), 268–276 (2009).
45. F. Bestvater, E. Spiess, G. Stobrawa, M. Hacker, T. Feurer, T. Porwol, U. Berchner-Pfannschmidt, C. Wotzlaw, and H. Acker, "Two-photon fluorescence absorption and emission spectra of dyes relevant for cell imaging," J. Microsc. **208**(Pt 2), 108–115 (2002).
46. P. S. Sheeran, S. Luois, P. A. Dayton, and T. O. Matsunaga, "Formulation and acoustic studies of a new phase-shift agent for diagnostic and therapeutic ultrasound," Langmuir **27**(17), 10412–10420 (2011).
47. N. Rapoport, Z. Gao, and A. Kennedy, "Multifunctional nanoparticles for combining ultrasonic tumor imaging and targeted chemotherapy," J. Natl. Cancer Inst. **99**(14), 1095–1106 (2007).
48. Z. Gao, A. M. Kennedy, D. A. Christensen, and N. Y. Rapoport, "Drug-loaded nano/microbubbles for combining ultrasonography and targeted chemotherapy," Ultrasonics **48**(4), 260–270 (2008).
49. O. D. Kripfgans, J. B. Fowlkes, D. L. Miller, O. P. Eldevik, and P. L. Carson, "Acoustic droplet vaporization for therapeutic and diagnostic applications," Ultrasound Med. Biol. **26**(7), 1177–1189 (2000).
50. O. Shpak, M. Verweij, N. de Jong, and M. Versluis, "Droplets, Bubbles and Ultrasound Interactions," Adv. Exp. Med. Biol. **880**, 157–174 (2016).
51. N. Y. Rapoport, A. L. Efros, D. A. Christensen, A. M. Kennedy, and K. H. Nam, "Microbubble Generation in Phase-Shift Nanoemulsions used as Anticancer Drug Carriers," Bubble Sci. Eng. Technol. **1**(1-2), 31–39 (2009).
52. N. Reznik, M. Seo, R. Williams, E. Bolewska-Pedyczak, M. Lee, N. Matsuura, J. Gariepy, F. S. Foster, and P. N. Burns, "Optical studies of vaporization and stability of fluorescently labelled perfluorocarbon droplets," Phys. Med. Biol. **57**(21), 7205–7217 (2012).
53. N. Rapoport, "Drug-Loaded Perfluorocarbon Nanodroplets for Ultrasound-Mediated Drug Delivery," Adv. Exp. Med. Biol. **880**, 221–241 (2016).
54. A. S. Kabalnov, K. N. Makarov, O. V. Shcherbakova, and A. N. Nesmeyanov, "Solubility of Fluorocarbons in Water as a Key Parameter Determining Fluorocarbon Emulsion Stability," J. Fluor. Chem. **50**(3), 271–284 (1990).
55. O. Ilina, L. Campanello, P. G. Gritsenko, M. Vullings, C. Wang, P. Bult, W. Losert, and P. Friedl, "Intravital microscopy of collective invasion plasticity in breast cancer," Dis. Model. Mech. **11**(9), dmm034330 (2018).
56. N. Rapoport, K. H. Nam, R. Gupta, Z. Gao, P. Mohan, A. Payne, N. Todd, X. Liu, T. Kim, J. Shea, C. Scaife, D. L. Parker, E. K. Jeong, and A. M. Kennedy, "Ultrasound-mediated tumor imaging and nanotherapy using drug loaded, block copolymer stabilized perfluorocarbon nanoemulsions," J. Control. Release **153**(1), 4–15 (2011).
57. N. Rapoport, D. A. Christensen, A. M. Kennedy, and K. H. Nam, "Cavitation properties of block copolymer stabilized phase-shift nanoemulsions used as drug carriers," Ultrasound Med. Biol. **36**(3), 419–429 (2010).
58. L. Kong, J. Tang, J. P. Little, Y. Yu, T. Lämmermann, C. P. Lin, R. N. Germain, and M. Cui, "Continuous volumetric imaging via an optical phase-locked ultrasound lens," Nat. Methods **12**(8), 759–762 (2015).
59. S. Pinner, P. Jordan, K. Sharrock, L. Bazley, L. Collinson, R. Marais, E. Bonvin, C. Goding, and E. Sahai, "Intravital imaging reveals transient changes in pigment production and Brn2 expression during metastatic melanoma dissemination," Cancer Res. **69**(20), 7969–7977 (2009).
60. D. R. Chittajallu, S. Florian, R. H. Kohler, Y. Iwamoto, J. D. Orth, R. Weissleder, G. Danuser, and T. J. Mitchison, "In vivo cell-cycle profiling in xenograft tumors by quantitative intravital microscopy," Nat. Methods **12**(6), 577–585 (2015).

Biomedical Optics EXPRESS

61. T. M. Kirrane and W. J. Middleton, "7-Amino-4-perfluoroheptylcoumarins: a novel class of perfluorocarbon-soluble fluorescent dyes," J. Fluor. Chem. **62**(2-3), 289–292 (1993).
62. S. K. Patel, M. J. Patrick, J. A. Pollock, and J. M. Janjic, "Two-color fluorescent (near-infrared and visible) triphasic perfluorocarbon nanoemuslions," J. Biomed. Opt. **18**(10), 101312 (2013).
63. E. M. Sletten and T. M. Swager, "Fluorofluorophores: fluorescent fluorous chemical tools spanning the visible spectrum," J. Am. Chem. Soc. **136**(39), 13574–13577 (2014).
64. J. Laudien, D. Naglav, C. Gro-Heitfeld, K. B. Ferenz, H. de Groot, C. Mayer, S. Schulz, A. Schnepf, and M. Kirsch, "Perfluorodecalin-soluble fluorescent dyes for the monitoring of circulating nanocapsules with intravital fluorescence microscopy," J. Microencapsul. **31**(8), 738–745 (2014).
65. D. Débarre, W. Supatto, A. M. Pena, A. Fabre, T. Tordjmann, L. Combettes, M. C. Schanne-Klein, and E. Beaurepaire, "Imaging lipid bodies in cells and tissues using third-harmonic generation microscopy," Nat. Methods **3**(1), 47–53 (2006).
66. S. Dietzel, J. Pircher, A. K. Nekolla, M. Gull, A. W. Brändli, U. Pohl, and M. Rehberg, "Label-free determination of hemodynamic parameters in the microcirculaton with third harmonic generation microscopy," PLoS One **9**(6), e99615 (2014).
67. R. K. Hartman, K. A. Hallam, E. M. Donnelly, and S. Y. Emelianov, "Photoacoustic imaging of gold nanorods in the brain delivered via microbubble-assisted focused ultrasound: a tool for in vivo molecular neuroimaging," Laser Phys. Lett. **16**(2), 025603 (2019).
68. N. B. Elsedawy and S. J. Russell, "Oncolytic vaccines," Expert Rev. Vaccines **12**(10), 1155–1172 (2013).
69. L. Hammerich, N. Bhardwaj, H. E. Kohrt, and J. D. Brody, "In situ vaccination for the treatment of cancer," Immunotherapy **8**(3), 315–330 (2016).
70. S. Lin, A. Shah, J. Hernández-Gil, A. Stanziola, B. I. Harriss, T. O. Matsunaga, N. Long, J. Bamber, and M. X. Tang, "Optically and acoustically triggerable sub-micron phase-change contrast agents for enhanced photoacoustic and ultrasound imaging," Photoacoustics **6**, 26–36 (2017).
71. D. A. Fernandes and M. C. Kolios, "Intrinsically absorbing photoacoustic and ultrasound contrast agents for cancer therapy and imaging," Nanotechnology **29**(50), 505103 (2018).
72. P. S. Sheeran and P. A. Dayton, "Improving the performance of phase-change perfluorocarbon droplets for medical ultrasonography: current progress, challenges, and prospects," Scientifica (Cairo) **2014**, 579684 (2014).
73. V. V. Tuchin, *Optical Clearing of Tissues and Blood* (SPIE Press, 2006), pp. xii, 254 p.
74. V. V. Tuchin, "Optical clearing of tissues and blood using the immersion method," J. Phys. D Appl. Phys. **38**(15), 2497–2518 (2005).
75. V. V. Tuchin, "Optical immersion as a new tool for controlling the optical properties of tissues and blood," Laser Phys. **15**, 1109–1136 (2005).
76. V. V. Tuchin, I. L. Maksimova, V. I. Kochubey, I. L. Kon, A. H. Mavlutov, A. A. Mishin, S. V. Tuchin, and D. A. Zymnyakov, "Optical and osmotic properties of human sclera," Optical Tomography and Spectroscopy of Tissue: Theory, Instrumentation, Model, and Human Studies Ii, Proceedings Of **2979**, 658–675 (1997).
77. V. V. Tuchin, I. L. Maksimova, D. A. Zimnyakov, I. L. Kon, A. K. Mavlutov, and A. A. Mishin, "Light propagation in tissues with controlled optical properties," P Soc Photo-Opt Ins **2925**, 118–142 (1996).
78. D. Zhu, K. V. Larin, Q. Luo, and V. V. Tuchin, "Recent progress in tissue optical clearing," Laser Photonics Rev. **7**(5), 732–757 (2013).
79. E. A. Calle, S. Vesuna, S. Dimitrievska, K. Zhou, A. Huang, L. Zhao, L. E. Niklason, and M. J. Levene, "The use of optical clearing and multiphoton microscopy for investigation of three-dimensional tissue-engineered constructs," Tissue Eng. Part C Methods **20**(7), 570–577 (2014).
80. E. Olson, M. J. Levene, and R. Torres, "Multiphoton microscopy with clearing for three dimensional histology of kidney biopsies," Biomed. Opt. Express **7**(8), 3089–3096 (2016).